Mechanical anisotropy of adherent cells probed by a three-dimensional magnetic twisting device

Shaohua Hu, Luc Eberhard, Jianxin Chen, J. Christopher Love, James P. Butler, Jeffrey J. Fredberg, George M. Whitesides and Ning Wang

Am J Physiol Cell Physiol 287:1184-1191, 2004. First published Jun 22, 2004;
doi:10.1152/ajpcell.00224.2004

AJP - Cell Physiology is dedicated to innovative approaches to the study of cell and molecular physiology. It is published 12 times a year (monthly) by the American Physiological Society, 9650 Rockville Pike, Bethesda MD 20814-3991. ISSN: 0363-6143, ESSN: 1522-1563. Visit our website at http://www.the-aps.org/.

Am J Physiol Cell Physiol 287: C1184–C1191, 2004.
First published June 22, 2004; doi:10.1152/ajpcell.00224.2004.

Mechanical anisotropy of adherent cells probed by a three-dimensional magnetic twisting device

Shaohua Hu,[1] Luc Eberhard,[3] Jianxin Chen,[1] J. Christopher Love,[2] James P. Butler,[1] Jeffrey J. Fredberg,[1] George M. Whitesides,[2] and Ning Wang[1]

[1]*Physiology Program, Harvard School of Public Health, Boston 02115;* [2]*Department of Chemistry and Chemical Biology, Harvard University, Cambridge, Massachusetts 02138; and* [3]*EOL Eberhard, CH-4104 Oberwil, Switzerland*

Submitted 6 May 2004; accepted in final form 16 June 2004

Hu, Shaohua, Luc Eberhard, Jianxin Chen, J. Christopher Love, James P. Butler, Jeffrey J. Fredberg, George M. Whitesides, and Ning Wang. Mechanical anisotropy of adherent cells probed by a three-dimensional magnetic twisting device. *Am J Physiol Cell Physiol* 287: C1184–C1191, 2004. First published June 22, 2004; doi:10.1152/ajpcell.00224.2004.—We describe a three-dimensional magnetic twisting device that is useful in characterizing the mechanical properties of cells. With the use of three pairs of orthogonally aligned coils, oscillatory mechanical torque was applied to magnetic beads about any chosen axis. Frequencies up to 1 kHz could be attained. Cell deformation was measured in response to torque applied via an RGD-coated, surface-bound magnetic bead. In both unpatterned and micropatterned elongated cells on extracellular matrix, the mechanical stiffness transverse to the long axis of the cell was less than half that parallel to the long axis. Elongated cells on poly-L-lysine lost stress fibers and exhibited little mechanical anisotropy; disrupting the actin cytoskeleton or decreasing cytoskeletal tension substantially decreased the anisotropy. These results suggest that mechanical anisotropy originates from intrinsic cytoskeletal tension within the stress fibers. Deformation patterns of the cytoskeleton and the nucleolus were sensitive to loading direction, suggesting anisotropic mechanical signaling. This technology may be useful for elucidating the structural basis of mechanotransduction.

cytoskeleton; prestress; stress fibers; mechanotransduction; mechanical deformation

LIVING CELLS AND TISSUES experience mechanical and chemical stimuli that are critical to their functioning. The mechanisms by which the cell responds to mechanical stimuli are less well understood than those of chemical stimuli (15, 18). This report describes the initial stages in characterizing how a cell responds to mechanical loads applied in different directions. A high ratio of length to width is critical for generating forces when striated muscle cells and smooth muscle cells contract, and cell polarity is also important for migration of nonmuscle cells (28). The formation of directed protrusions from elongated cells is crucial in neural tube development (7). At the subcellular level, individual cytoskeletal filaments, which define cell shape, have a length-to-width ratio greater than 10-100:1 (16). The cytoskeletal lattice is a complex, dynamic network with interacting filaments oriented in many different directions (19), but the extent to which living, adherent cells are mechanically anisotropic is unknown.

Various tools have been used to deform living cells, including microrods and cell poking, micropipette aspiration, elastomeric substrates, microchannels and fluid shear, scanning probe microscopes, and optical traps (1, 4, 6, 8, 9, 13, 27, 32). Magnetic particles attached to the cell surface can be manipulated using magnetic field gradients (2, 5), and the manipulations can include linear or oscillating forces or torques involving rotation of up to 90° (34, 35). The magnetic and optical approaches are among the most versatile because the probes can be coated with specific ligands and a wide range of force amplitudes and frequencies can be applied; they have been useful in characterizing the rheological properties of cells and the pathways by which cells transduce forces (2, 3, 10, 11, 17, 20, 21, 34–37). All of these approaches are limited, however, in the range of motions that can be used to apply force; therefore, they are not ideally suited to characterize the mechanical anisotropy of the cell.

MATERIALS AND METHODS

Cell culture. Human airway smooth muscle cells were serum deprived for 24 h and cultured on ligand-coated dishes overnight in serum-free medium according to previously published methods (37). Ferrimagnetic beads of 4.5-μm, 6-μm, or 200-nm diameter were used: the first two sizes of beads were produced in our laboratory, and the 200-nm beads were obtained from Polysciences (Warrington, PA). Superparamagnetic beads of 4.5-μm diameter were obtained from Dynal (Oslo, Norway). These paramagnetic particles do not retain any remnant magnetization. Yellow fluorescent protein (YFP)-actin, YFP-cytochrome *c* oxidase (in mitochondria), and green fluorescent protein (GFP)-caldesmon were transiently transfected into the cells according to previously published methods (17, 36). The magnetic beads were coated with saturated amounts of Arg-Gly-Asp (RGD)-containing peptides. This protocol induced a firm focal adhesion surrounding the bead. Binding specificity and magnetic moments were determined according to previously published methods (35).

Three-dimensional magnetic device. Our three-dimensional (3-D) magnetic twisting cytometer contains the following seven components: *1*) a high-voltage generator for generating the current in the coils used to magnetize the magnetic particles, *2*) three separate bipolar current sources to twist the particles, *3*) a personal computer to control the twisting, *4*) an inverted microscope to observe the sample, *5*) a charge-coupled device camera using self-written software to synchronize image capture with oscillatory magnetic fields, *6*) a temperature controller for living cells, and *7*) a microscope insert (see Fig. 6 in the APPENDIX).

To assess surface deformation induced by the rotating bead, the rotation-induced lateral movement of the bead center synchronized with the input torque was determined as the bead displacement using an intensity-weighted center-of-mass algorithm (11). Displacements of the cytoskeleton (CSK) and the nucleolus were quantified using a synchronous detection method (17). These displacements were phase-

Address for reprint requests and other correspondence: N. Wang, Physiology Program, Harvard School of Public Health, 665 Huntington Ave., Boston, MA 02115 (E-mail: nwang@hsph.harvard.edu).

The costs of publication of this article were defrayed in part by the payment of page charges. The article must therefore be hereby marked "*advertisement*" in accordance with 18 U.S.C. Section 1734 solely to indicate this fact.

locked with the sinusoidal mechanical input at a given frequency. The cells were maintained at 37°C during the experiments.

To estimate noise associated with the microscope stage, we determined the rigid body displacement by quantifying movements of a magnetic bead embedded in epoxy in the absence of an external load: at 125 ms/frame, the standard deviation of *x* displacement was 1.3 ± 0.02 nm and that of *y* displacement was 1.1 ± 0.1 nm (means ± SE). Thermal noise was ~10 nm in living cells for YFP mitochondria or the nucleolus. Taking advantage of the periodicity of the sinusoidal inputs, we averaged 5–10 cycles of images of data to improve the signal-to-noise ratio for the YFP mitochondria and the nucleolus. The noise floor was reduced to ~4 nm after averaging nine cycles of images and all load-induced displacements were synchronized with the frequency of the applied load at 0.3125 Hz (see Fig. 8 in the APPENDIX). The signal-to-noise ratio <2:1 for the YFP mitochondria or <1:1 for the nucleolus and 4 nm were chosen as the cutoff values (see Fig. 5).

Because the computer requires 120 ms to capture and store each 60 × 60-μm image, the heterodyning approach was used for >1 Hz to take advantage of the periodic feature of sinusoidal loading; e.g., only one image was obtained every 220 ms (1 cycle + ⅒ cycle) for the 5 Hz case and every 121.1 ms (121 cycles + ⅒ cycle) for the 10 Hz case. The camera-triggering time was synchronized with loading input and 10 images were obtained, resulting in a 36° rotation between successive images for all frequencies.

Micropatterning technique. Polydimethylsiloxane (PDMS) membranes were made using photolithography according to procedures described previously (25). Briefly, PDMS membranes with the same area (~2,500 μm^2) holes but different shapes were fabricated: either 56-μm diameter circles, or 125 × 20-μm and 156 × 16-μm rectangles (length-to-width ratios of 6.25 and 9.75, respectively; normal airway smooth muscle cell length-to-width ratio is >6:1). We coated the plastic dishes with extracellular matrix (ECM) molecules (type 1 collagen, 40 μg/ml) or poly-L-lysine (40 μg/ml) through the holes of the membranes sealed onto the dishes overnight and then lifted off the membrane. After blocking the rest of the dish area with 1% BSA, we plated cells sparsely overnight. Single cells that assumed circular or rectangular shapes of the same area were used for obtaining mechanical measurements.

RESULTS AND DISCUSSION

We describe a system that can rotate a magnetic bead along any axis. We call this device a 3-D magnetic twisting cytometer, or 3-D MTC. This device uses pairs of coils oriented along three orthogonal axes and controls the amplitude, frequency, and phase in each pair independently (Fig. 1*A*; see also Fig. 6 in the APPENDIX). Each pair of coils is capable of producing a homogeneous magnetic field in its axial direction, with a nearly zero radial component and negligible field gradients over the diameter of the coil (see Fig. 7 in the APPENDIX). Thus, in its rotational mode, it can generate pure torque with no linear component of force. The device can magnetize beads with a moment vector M by applying a strong, short magnetic pulse [~1,000 G (0.1 Tesla) for ~0.5 ms] via any coil pair. Subsequently, it can apply a weak twisting field vector B via another coil pair (0–25 G, too weak to remagnetize the beads) to generate a torque *T* on the beads with complete orientational freedom of vectors M and B.

Continuous rotation of magnetic beads about any axis. After 4.5-μm ferrimagnetic beads were magnetized in the *y* direction by applying a strong magnetic pulse via the *y* coil pair, the beads were continuously rotated clockwise about the *z*-axis (i.e., in the *x*-*y* plane) by simultaneously applying two sinusoidal fields of 25 G (2.5 mT) at 0.5 Hz in both *x* and *y* with a 90° phase lag (Fig. 1*B*, *top row*). Smaller (200 nm) beads were also rotated in this manner (data not shown). A pair of superparamagnetic beads rotated at 5 Hz by simply applying a sinusoidal alternating current field; it was not necessary to magnetize the pair before twisting them (Fig. 1*B*, *second row*). The magnetic beads could rotate at frequencies up to 1,000 Hz (Fig. 1*B*, *third row*). The direction of rotation was easily changed from clockwise to counterclockwise by switching the 90° phase lag in the *y* direction to a 90° phase lead. Similarly, the beads could also be rotated about the *y*-axis by magnetizing the bead, first along the *x*-axis and then by simultaneously applying alternating current fields in the *z* and *x* directions with a 90° phase lag or lead. By simultaneously applying fields in all three directions

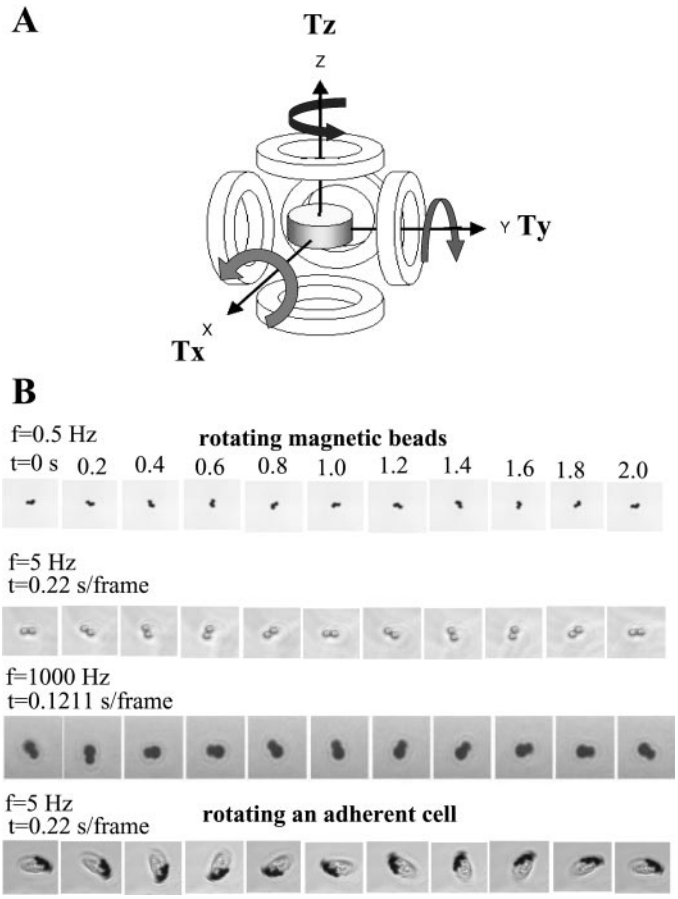

Fig. 1. *A*: schematic (not to scale) of the 3-dimensional (3-D) magnetic twisting device (3-D MTC) with 3 pairs of orthogonally aligned coils to produce homogeneous magnetic fields and torque *T* about the *x*- (T_x), *y*- (T_y), and *z*-axes (T_z) independently (curved arrows represent bead rotation directions). The front *x* coil is omitted for clarity of view. The sample is at the center and is located at the focal plane of the microscope. *B*: continuous rotation of magnetic beads in biological medium in *x*-*y* plane in response to T_z. *Top row*: 360° rotation of a 4.5-μm ferrimagnetic bead aggregate (3 beads) at 0.5 Hz. After magnetization in the *y* direction, bead rotation was achieved by simultaneously applying a sinusoidal twisting field in the *x* and *y* directions with a 90° phase lag in *y*. Magnetic field amplitude was 25 G, and specific torque was 45 Pa. *Second row from top*: pair of 4.5-μm superparamagnetic beads rotated completely in response to the same *x*-*y* field combination at 5 Hz without magnetization (10-ms camera exposure time). *Third row from top*: pair of 6-μm ferrimagnetic beads rotated at 1,000 Hz (50-μs camera exposure time). *Bottom row*: adherent spread cell bound to a 5-bead aggregate was rotated at 5 Hz, possibly after adhesion sites were broken by the applied torque. Magnification, ×200 in *top*, *second*, and *bottom rows* and ×400 in *third row*.

with appropriate phase lags, more complex patterns of bead rotation were achieved (data not shown). An adherent cell bound to an RGD-coated bead aggregate was rotated at 5 Hz (Fig. 1*B*, *bottom row*), possibly after adhesion contacts were broken by the applied torque. Our results also suggest that, when they are bound to a magnetic bead, molecules (e.g., DNA) and cellular structures (e.g., flagella) may be rotated about any axis at high speed.

Mechanical anisotropy depends on stress fiber orientation and cytoskeletal tension. We examined the relationship between the direction of mechanical loads applied to an elongated cell and the structure of the CSK. We applied an oscillating torque (45 Pa at 0.83 Hz, a physiological load that produced an average cellular surface deformation ~0.15 ± 0.03 μm) to a single RGD-coated spherical bead attached to the apical surface of human airway smooth muscle cells via integrin receptors in two different ways: *1*) the bead was magnetized (M) in the *x* direction, and a twisting field B was applied in the *z* direction: this combination of fields induced a torque *T* about the *y*-axis (T_y) (Fig. 2*A*, *left bead*); and *2*) the bead was magnetized in the *y* direction, and a twisting field was applied in the *z* direction: this combination induced a torque *T* about the *x*-axis (T_x) (Fig. 2*A*, *right bead*).

When the applied torque T_y and the long axis of the cell were parallel (i.e., in the *y* direction), the principal direction of motion of the bead was perpendicular to the long axis of the cell. The displacement was approximately twofold that observed in a corresponding experiment in which the axis of torque T_x was perpendicular to the long axis (Fig. 2*B*, shaded bars). In contrast, when the long axis of the cell was perpendicular to the applied torque T_y, the displacement of the bead was greater in response to T_x than to T_y (Fig. 2*B*). Using a loading frequency of 0.3 Hz produced similar results. These experiments indicate that, for a given torque, it was easier to deform the cell by rotating the bead perpendicular to the long axis of the cell than by rotating it parallel to the long axis. Furthermore, these data suggest that the mechanical stiffness of an elongated smooth muscle cell depends on the direction of the load relative to the long axis of the cell. The mechanical anisotropic behavior of these cells represents substantial departures from the cell model of isotropic viscoelasticity (14) and is also distinct from the cellular behavior of mechanical heterogeneity (2, 27).

We hypothesized that the structure of the CSK might influence mechanical anisotropy. To test this hypothesis, we disrupted the F-actin in the CSK of the cells using two different drugs: latrunculin A (Fig. 2*C*) and cytochalasin D (Fig. 2*C*). Within 3 min of adding the drug to the medium, and in the absence of changes in cell shape, exposure to either drug resulted in greatly increased displacements of the bead (at constant magnetic torque) and almost completely abolished mechanical anisotropy (Fig. 2*C*). These data suggest that F-actin is involved in determining the mechanical anisotropy.

To control the projected area and shape of the cell and to explore further the underlying origin of the observed mechanical anisotropy, we plated cells on micropatterned islands having the same area (~2,500 μm^2, an area chosen on the basis of normal projected areas of smooth muscle cells), but with different shapes and different length-to-width aspect ratios. We applied a constant magnetic torque to a magnetic bead and measured the displacement both parallel and perpendicular to the long axis of these patterned cells. We define the "anisotropy index" as the ratio of stiffness, that is, the specific torque (torque per bead volume or apparent stress) divided by dis-

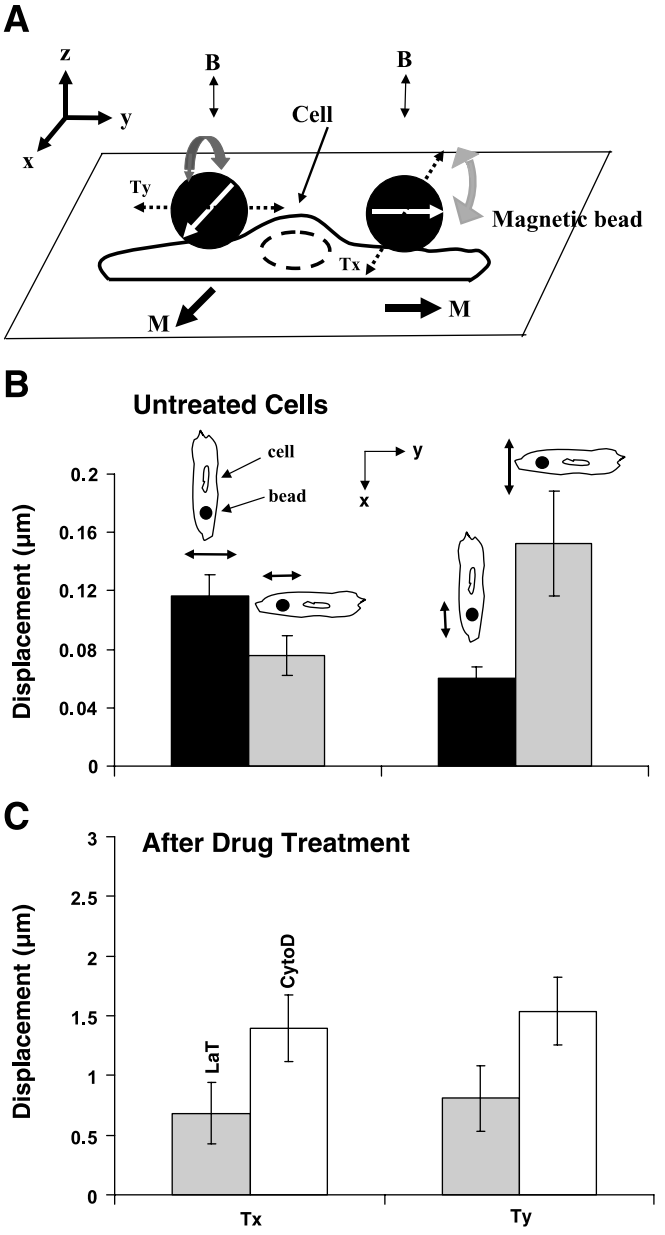

Fig. 2. Cell deformation in response to torque applied about different axes. *A*: schematic of a torque applied to a cell along 2 different directions. *Left* bead (not drawn to scale) rotated in the *x*-*z* plane (curved double arrow, not to scale) in response to T_y (dashed arrows) generated by a twisting field B in *z* after magnetization M in *x*. *Right* bead rotated in the *y*-*z* plane (curved double arrow, not to scale) in response to T_x (dashed arrows) generated by a twisting field B in *z* after magnetization M in *y*. *B*: data from normal untreated smooth muscle cells plated on collagen-1-coated dishes. The cell's long axis was positioned along the *x* direction (solid bars, $n = 25$ cells; $P < 0.000006$) or along the *y* direction (shaded bars, $n = 17$ cells; $P < 0.02$). Solid dots represent a magnetic bead inside a cell (not drawn to scale); double arrows represent bead rotation directions. All *t*-tests are paired tests of displacements in 2 different directions. *C*: data from cells after drug treatments. LaT, latrunculin A (1 μM for 3 min) ($n = 12$ cells; $P > 0.08$, not significantly different); CytoD, cytochalasin D (1 μg/ml for 3 min) ($n = 14$ cells; $P > 0.44$, not significantly different). Note that displacements increased greatly, indicating that cell stiffness decreased dramatically.

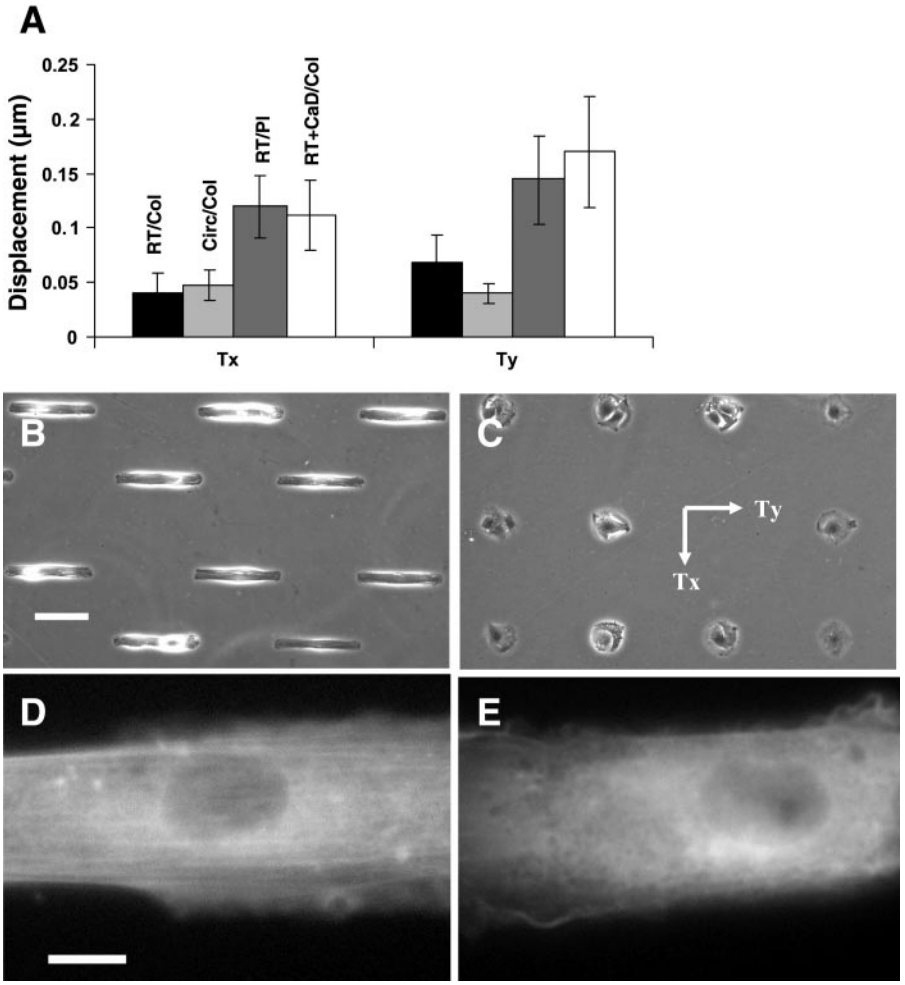

Fig. 3. Deformation of cells plated on micropatterned islands of the same area (2,500 μm^2). *A*: All cells' long axes aligned along the *y* direction. RT/Col: cells on collagen-1 coated rectangular islands (n = 20 cells, $P < 0.03$); Circ/Col: cells on collagen-1-coated circular islands (n = 14 cells; $P > 0.25$, not significantly different); RT/Pl: cells on poly-L-lysine-coated rectangular islands (n = 17 cells, $P > 0.12$, not significantly different); RT+CaD/Col: caldesmon-transfected cells on collagen-1-coated rectangular islands (n = 18 cells; $P < 0.05$). *B*: phase-contrast image of micropatterned rectangular cells (length-to-width ratio is 9.75:1). *C*: phase-contrast image of micropatterned round cells. *D*: fluorescence microscopic image of a yellow fluorescent protein (YFP)-actin-transfected, micropatterned cell plated on collagen-1, showing numerous actin stress fibers and/or bundles along the long axis of the cell. *E*: fluorescence microscopic image of a YFP-actin-transfected, micropatterned cell plated on poly-L-lysine, lacking stress fibers and/or actin bundles. Scale bars, 100 μm (*B* and *C*) and 10 μm (*D* and *E*).

placement along the long axis of the cell to the stiffness transverse to the long axis of the cell. An index of 1.0 indicates that the mechanical response is isotropic. The cells plated on ECM-coated rectangular islands (Fig. 3*B*; aspect ratio 9:1) had anisotropic mechanical behavior, because the deformation was twice as large when the bead rotated across (i.e., transverse to) the long axis of the cell than when the bead rotated along (i.e., parallel to) the long axis (Fig. 3*A*). The anisotropy index was 2.1 ± 0.3 ($P < 0.007$ vs. isotropy or index of 1.0) and similar to that of unpatterned, natural cells, which was 2.0 ± 0.2 ($P < 0.00003$ vs. isotropy) (Fig. 4). In contrast, the stiffness of the cells plated on circular islands of ECM (Fig. 3*C*; aspect ratio 1:1) did not depend on the direction of the applied torque and thus exhibited no mechanical anisotropy (Fig. 3*A*). These results are consistent with recent results at our laboratory demonstrating deep cytoskeletal anisotropy detected by differential phase lags in *x* vs. *y* directions (17), with a recent report showing that cyclically strained adherent cells are stiffer along the long axis (33), and with the finding of an anisotropic strain in the erythrocyte cortical CSK in response to a large deformation (22). It remains to be seen, however, to what degree these smooth muscle cells in a 3-D culture environment and other elongated nonmuscle cells (e.g., endothelial cells and epithelial cells) exhibit mechanical anisotropy.

When cells were plated on micropatterned rectangular islands coated with poly-L-lysine instead of ECM, the anisotropy index decreased to 1.2 ± 0.1 ($P > 0.07$), which is not significantly different from 1.0 or the isotropic case (Fig. 4), even though the shapes and surface areas of the cells were indistinguishable from those on ECM (compare Fig. 3, *D* with

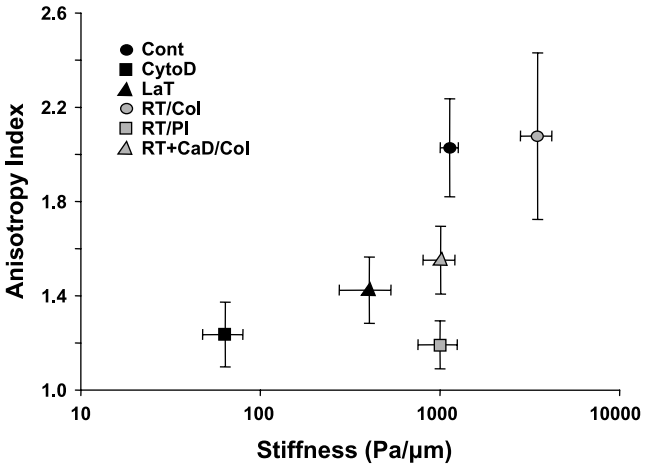

Fig. 4. Anisotropy index as a function of stiffness along the long axis under different experimental conditions. Stiffness is defined as specific torque per deformation. Cont: unpatterned cells on collagen-1 (n = 30 cells). Other cell numbers and letter symbols are the same as those defined in Figs. 2 and 3. Data are means ± SE. RT/Col cells were stiffer than control cells, possibly because of perfect alignment and/or transfection of YFP-actin into those cells.

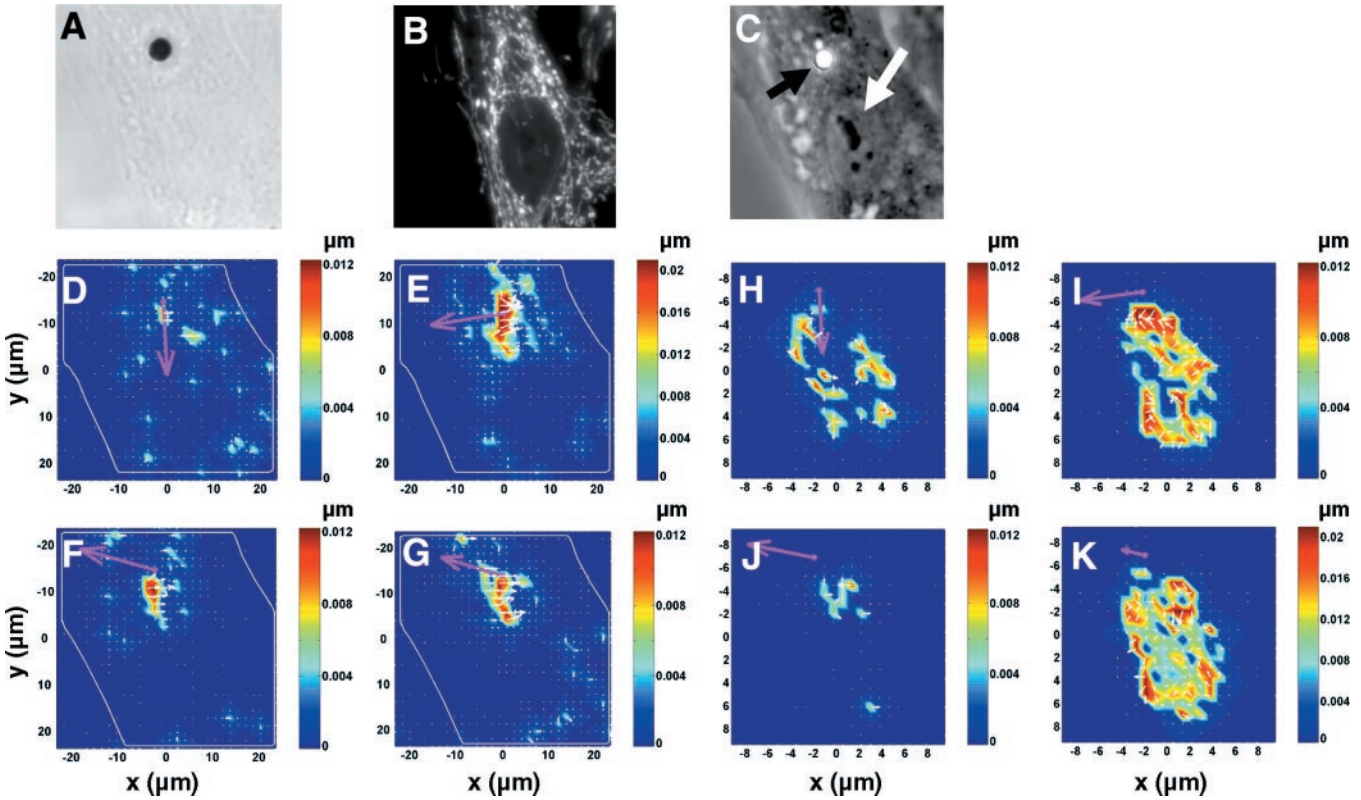

Fig. 5. Mechanical signaling to the cytoskeleton (CSK) and to the nucleolus. *A*: magnetic bead (5.4 μm diameter) on the surface of an elongated cell aligned mostly along the *x* direction. *B*: fluorescence microscopic image of YFP-mitochondria of the same cell (focal plane at ~2 μm above cell base). *C*: phase-contrast image showing the nucleolus (large white arrow) and the bead (black arrow) of the same cell. *D* and *H*: displacement maps of the CSK (*D*) and of the nucleolus (*H*) in response to a torque (45 Pa at 0.83 Hz) applied along the *y* direction (see Fig. 2*A*). *E* and *I*: displacement maps of the CSK (*E*) and of the nucleolus (*I*) in response to the same torque applied along the *x* direction (see Fig. 2*B*). *F*, *G*, *J*, and *K*: displacement maps of the CSK (*F* and *G*) and of the nucleolus (*J* and *K*) in response to torques applied simultaneously along 3 axes (all at 45 Pa and 0.83 Hz) with different phase lags ($x = 0°$, $y = 90°$, and $z = 0°$ in *F* and *J*; $x = 0°$, $y = 90°$, and $z = 90°$ in *G* and *K*; the bead was magnetized in the *y* direction in both cases). Color represents the magnitude, and small white arrows represent the direction, of the displacements. The distance between the bead front edge to the proximal end of the nucleolus is 11.8 μm. Pink arrow represents the position (not to scale in the nucleolar displacement maps) and direction of the bead center movement. Note that the patterns of the maps are quite different for different loading directions. Compare *D* with *E*, *H* with *I*, *F* with *G*, and *J* with *K*, although the load magnitude and frequency remained constant for each pair. Repeated applications of the same torque along the same direction did not result in changes in displacement patterns. Three other cells also exhibited altered patterns of displacement of the CSK and of the nucleolus in response to different loading directions.

E). Because cells plated on dishes coated with poly-L-lysine lose focal adhesions and stress fibers and/or actin bundles (24) (Fig. 3*E*), these data suggest that the presence of stress fibers and/or actin bundles (Fig. 3*D*), inherently oriented along the long axis of the cell, and not the elongated cell shape per se, is responsible for the mechanical anisotropy. We further quantified stress fiber orientation relative to the long axis of the cell in YFP-actin-transfected, unpatterned, elongated cells plated on ECM. We found that 78.5% of the stress fibers and/or actin bundles were oriented 0–10° relative to the long axis of the cell, 16.7% were oriented 15–25°, and 4.8% were aligned >30° [accuracy was approximately ±2.5°, $n = 12$ cells, 15.5 ± 2.4 (mean ± SE) stress fibers per basal focal plane per cell]. The hypothesis that stress fibers oriented along the long axis are responsible for mechanical anisotropy is compatible with the observation that disrupting the network of actin filaments in the CSK with latrunculin A or cytochalasin D, without changing the shape of the cell, decreased the anisotropy index to 1.4 ± 0.1 ($P < 0.01$ vs. isotropy) and 1.2 ± 0.1

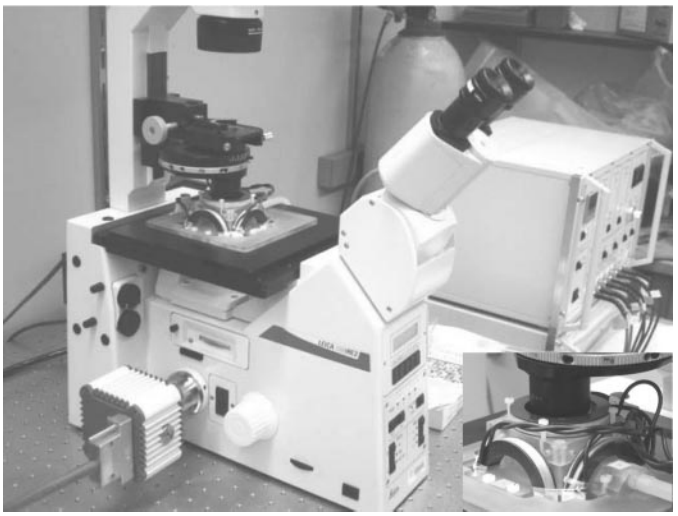

Fig. 6. 3-D MTC device. Close-up of the microscope insert with the temperature control tubing on the right corner is shown at *lower right corner* of the photograph.

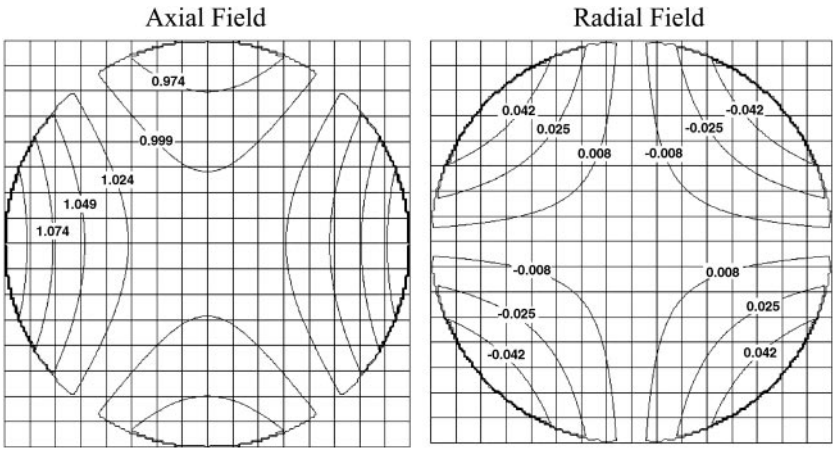

Fig. 7. Contour plots of axial field component (*left*) and radial field component (*right*) generated by 1 pair of coils at 1-A current. The coils are at left and right sides of the diagram; i.e., the magnetic axis is horizontal. A circular region of 16-mm diameter is shown, grid spacing is 1 mm, and magnetic induction is given in mT. Note that the axial field has a nearly uniform 1-mT field, whereas the radial field is nearly 0.

($P > 0.1$ vs. isotropy, not significantly different from 1.0), respectively, for elongated cells on ECM (Fig. 2*C*, Fig. 4).

Recently, researchers at our laboratory have shown that endogenous cytoskeletal tension (i.e., prestress) dictates cell stiffness (36, 37). To test further the hypothesis that the tension in the stress fibers and/or actin bundles along the long axis of the cell contributes to the mechanical anisotropy of the cell, we transfected caldesmon into the cell. Caldesmon decreases cytoskeletal tension by inhibiting the interaction between actin and myosin (24). Transfecting a low level of caldesmon into the cell decreased cytoskeletal tension by 50% without altering the shape of the cell, the distribution of focal adhesions, or stress fibers (17, 24). Interestingly, these cells also exhibited lower mechanical anisotropy than the wild type; the anisotropy index decreased from 2.1 to 1.6 ± 0.1 ($P < 0.0005$ vs. isotropy). This difference represents a 45% decrease in anisotropy (a 100% decrease in anisotropy would be equivalent to an anisotropy index of 1.0) (Fig. 3*A*, open bars; Fig. 4).

We note that decreasing the cytoskeletal tension by overexpressing caldesmon and abolishing stress fibers by plating the cells on poly-L-lysine decreased the anisotropy index from ~2 toward 1 (i.e., isotropy) while decreasing stiffness by a factor of 3 in micropatterned cells (Fig. 4). Similarly, when the CSK was disrupted with drugs, there was a shift from anisotropy toward isotropy, a threefold decrease in stiffness after treating the cells with latrunculin A, and a >10-fold decrease in stiffness after treatment with cytochalasin D in unpatterned cells (Fig. 4). These observations suggest that the common structural origin of mechanical anisotropy in these living cells is the preferential orientation of stress fibers and/or actin bundles along the long axis of the cell.

Anisotropic mechanical signaling to the CSK and to the nucleolus. To explore further the utility of 3-D MTC in intracellular mechanical signaling, using a recently developed synchronous detection method (17), we mapped the cytoskeletal displacement field of an elongated cell (Fig. 5*A*) with transfected YFP-mitochondria as fiducial markers (17, 36) (Fig. 5*B*). The load-induced displacement patterns of the CSK were quite different in response to the applied torque of the same magnitude and frequency, but along different directions (compare Fig. 5*D* in response to T_y with Fig. 5*E* in response to T_x). Interestingly, when a more complex load was applied with all three oscillatory twisting fields switched on simultaneously with different phase lags ($x = 0°$, $y = 90°$, $z = 0°$ in Fig. 5*F*, or $x = 0°$, $y = 90°$, $z = 90°$ in Fig. 5*G*, respectively), distinctly different displacement patterns emerged (compare Fig. 5*F* with Fig. 5*G*). All of these results demonstrate that spatial distributions of the cytoskeletal deformation depend on not only on the magnitude and frequency but also the direction of loading.

We next mapped the displacements of the nucleolus, an intranuclear organelle crucial for ribosomal RNA synthesis (31), in response to the load applied at the cell surface. The nucleolus of an interphase cell is visible under phase-contrast microscopy without staining or GFP (Fig. 5*C*). The displacement map within the nucleolus varied with the loading direction: changing the torque direction by 90° (from T_y in Fig. 5*H*

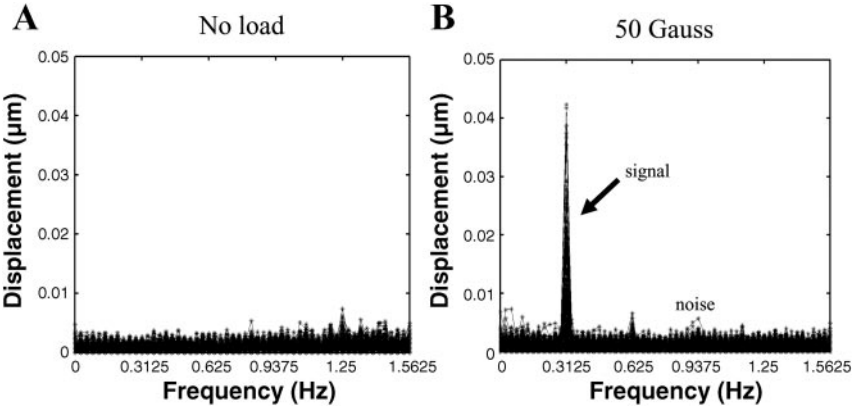

Fig. 8. Noise analysis of mitochondrial displacement in an individual cell under baseline conditions. *A*: single Arg-Gly-Asp (RGD) bead was bound to the cell apical surface in the presence of a near-zero mechanical load (twisting field = 0.5 G at 0.3125 Hz); *B*: single RGD bead was bound to the cell apical surface in the presence of a 50-G sinusoidal twisting field at 0.3125 Hz. Each curve in the graph represents a frequency spectrum of mitochondrial displacements from a 1 × 1-μm area.

to T_x in Fig. 5*I*) drastically altered displacement patterns of the nucleolus. Applying a complex load, with all three twisting fields switched on simultaneously with different phase lags, led to dramatically different nucleolar displacement maps (compare Fig. 5*J* with Fig. 5*K*): concentrated displacements occurred at different sites and pointed in various directions within the nucleolus, demonstrating different intranucleolar deformation patterns. These results suggest that physiological loads applied at the cell surface might be able to regulate and control nuclear functions directly (e.g., synthesis of ribosomal RNA) via the structural pathways of the CSK and the nuclear matrix. The specific biological responses of the nucleus may therefore depend on the direction of mechanical loading. This result, together with the result of cytoskeletal deformation, extends the previous finding of Maniotis et al. (23) and demonstrates that small but physiologically relevant surface deformation applied via integrin receptors along different directions can elicit different mechanical deformation patterns deep in the cytoplasm and in the nucleus.

In summary, we demonstrate that elongated adherent cells exhibit intrinsic mechanical anisotropy. This anisotropy may originate in the prestress residing in stress fibers and/or actin bundles oriented preferentially along the long axis of the cell. We also show that intracellular deformation patterns of the CSK and the nucleolus are sensitive to directions of loading. Much of the current research on the mechanics of the cell focuses on elucidating mechanotransduction pathways at the cell surface and especially in elucidating the role of focal adhesions (12, 29). Our results regarding intracellular anisotropic mechanical signaling suggest that load direction-dependent direct mechanotransduction may also occur deep in the cytoplasm and inside the nucleus via the structural pathways of the CSK and within the nucleus (17, 23). We think that this new mechanical loading device will be a valuable tool for probing mechanisms of mechanotransduction when used in combination with single live cell biochemical assays (30, 38).

APPENDIX

The microscope insert consists of a set of three pairs of coils arranged at right angles around the sample site (Fig. 6). The insert with its three pairs of coils thus defines a spatial coordinate system with Cartesian coordinate system of *x*, *y*, and *z* axes. The *x*- and *y*-axes lie in the plane of the microscope stage, and the *z*-axis coincides with the optical axis of the microscope. Each coil pair can be used for both magnetization and twisting. The coils are 51 mm in diameter, grouped into three pairs, and separated by 70 mm in distance. This is an approximation of the Helmholtz configuration: each pair of coils produces a nearly homogeneous magnetic field in its axial direction within the small field of view of the microscope (Fig. 7). Thus nearly pure torque with negligible lateral force was applied to the magnetic beads, owing to negligible magnetic field gradient (Fig. 7). The coils have 100 turns, each of which leads to inductance of 1.43 mH per pair and a central plane magnetic induction of 1 mT (10 G) per ampere of current. To magnetize the bead, a 16-μF capacitor is charged by a high-voltage generator up to 2.7 kV. The resulting magnetizing pulse is ~470 μs and has an amplitude of up to 285 mT (2.8 kG). The voltage compliance is 40 V bipolar. This value gives a maximum rate of current change of 28 kA/s with the 1.43 mH inductance of the coil pairs. This protocol allows for the generation of 2.2-A peak sinusoidal current at a frequency up to 2 kHz.

ACKNOWLEDGMENTS

We thank D. E. Ingber for GFP-caldesmon constructs and R. A. Panettieri Jr. for providing the human airway smooth muscle cells.

GRANTS

This work was supported by National Aeronautics and Space Administration Grant NAG2–1509, National Heart, Lung, and Blood Institute Grants HL-33009 and HL-65960, and a grant from the Defense Advanced Research Projects Agency.

REFERENCES

1. **Banes AJ, Gilbert J, Taylor D, and Monbureau O.** A new vacuum-operated stress-providing instrument that applies static or variable duration cyclic tension or compression to cells in vitro. *J Cell Sci* 75: 35–42, 1985.
2. **Bausch AR, Möller W, and Sackmann E.** Measurement of local viscoelasticity and forces in living cells by magnetic tweezers. *Biophys J* 76: 573–579, 1999.
3. **Chen Z, Bao G, and Wang N.** Cell mechanics: mechanical response, cell adhesion, and molecular deformation. *Annu Rev Biomed Eng* 2: 189–226, 2000.
4. **Chien S, Sung KLP, Skalak R, Usami S, and Tozeren A.** Theoretical and experimental studies on viscoelastic properties of erythrocyte membrane. *Biophys J* 24: 463–487, 1978.
5. **Crick FHC and Hughes AFW.** The physical properties of cytoplasm: a study by means of the magnetic particle method. *Exp Cell Res* 1: 37–80, 1950.
6. **Dai J and Sheetz MP.** Mechanical properties of neuronal growth cone membranes studied by tether formation with laser optical tweezers. *Biophys J* 68: 988–996, 1995.
7. **Davidson LA and Keller RE.** Neural tube closure in *Xenopus laevis* involves medial migration, directed protrusive activity, cell intercalation and convergent extension. *Development* 126: 4547–4556, 1999.
8. **Davies PF, Robotewskyj A, and Griem ML.** Endothelial cell adhesion in real time: measurements in vitro by tandem scanning confocal image analysis. *J Clin Invest* 91: 2640–2652, 1993.
9. **Evans E and Yeung A.** Apparent viscosity and cortical tension of blood granulocytes determined by micropipet aspiration. *Biophys J* 56: 151–160, 1989.
10. **Fabry B, Maksym GN, Butler JP, Glogauer M, Navajas D, and Fredberg JJ.** Scaling the microrheology of living cells. *Phys Rev Lett* 87: 148102, 2001.
11. **Fabry B, Maksym GN, Shore SA, Moore PE, Panettieri RA Jr, Butler JP, and Fredberg JJ.** Selected contribution: time course and heterogeneity of contractile responses in cultured human airway smooth muscle cells. *J Appl Physiol* 91: 986–994, 2001.
12. **Felsenfeld DP, Schwartzberg PL, Venegas A, Tse R, and Sheetz MP.** Selective regulation of integrin-cytoskeleton interactions by the tyrosine kinase Src. *Nat Cell Biol* 1: 200–206, 1999.
13. **Guck J, Ananthakrishnan R, Mahmood H, Moon TJ, Cunningham CC, and Käs J.** The optical stretcher: a novel laser tool to micromanipulate cells. *Biophys J* 81: 767–784, 2001.
14. **Heidemann SR, Kaech S, Buxbaum RE, and Matus A.** Direct observations of the mechanical behaviors of the cytoskeleton in living fibroblasts. *J Cell Biol* 145: 109–122, 1999.
15. **Heidemann SR and Wirtz D.** Towards a regional approach to cell mechanics. *Trends Cell Biol* 14: 160–166, 2004.
16. **Heuser JE and Kirschner MW.** Filament organization revealed in platinum replicas of freeze-dried cytoskeletons. *J Cell Biol* 86: 212–234, 1980.
17. **Hu S, Chen J, Fabry B, Numaguchi Y, Gouldstone A, Ingber DE, Fredberg JJ, Butler JP, and Wang N.** Intracellular stress tomography reveals stress focusing and structural anisotropy in the cytoskeleton of living cells. *Am J Physiol Cell Physiol* 285: C1082–C1090, 2003.
18. **Ingber DE.** Mechanobiology and diseases of mechanotransduction. *Ann Med* 35: 564–577, 2003.
19. **Janmey PA.** The cytoskeleton and cell signaling: component localization and mechanical coupling. *Physiol Rev* 78: 763–781, 1998.
20. **Jiang G, Giannone G, Critchley DR, Fukumoto E, and Sheetz MP.** Two-piconewton slip bond between fibronectin and the cytoskeleton depends on talin. *Nature* 424: 334–337, 2003.
21. **Kuo SC.** Using optics to measure biological forces and mechanics. *Traffic* 2: 757–763, 2001.

22. **Lee JCM, Wong DT, and Discher DE.** Direct measures of large, anisotropic strains in deformation of the erythrocyte cytoskeleton. *Biophys J* 77: 853–864, 1999.
23. **Maniotis A, Chen CS, and Ingber DE.** Demonstration of mechanical connections between integrins, cytoskeletal filaments, and nucleoplasm that stabilize nuclear structure. *Proc Natl Acad Sci USA* 94: 849–854, 1997.
24. **Numaguchi Y, Huang S, Polte TR, Eichler GS, Wang N, and Ingber DE.** Caldesmon-dependent switching between capillary endothelial cell growth and apoptosis through modulation of cell shape and contractility. *Angiogenesis* 6: 55–64, 2003.
25. **Ostuni E, Kane R, Chen CS, Ingber DE, and Whitesides GM.** Patterning mammalian cells using elastomeric membranes. *Langmuir* 16: 7811–7819, 2000.
26. **Paterson L, MacDonald MP, Arlt J, Sibbett W, Bryant PE, and Dholakia K.** Controlled rotation of optically trapped microscopic particles. *Science* 292: 912–914, 2001.
27. **Petersen NO, McConnaughey WB, and Elson EL.** Dependence of locally measured cellular deformability on position on the cell, temperature, and cytochalasin B. *Proc Natl Acad Sci USA* 79: 5327–5331, 1982.
28. **Ridley AJ, Schwartz MA, Burridge K, Firtel RA, Ginsberg MH, Borisy G, Parsons JT, and Horwitz AR.** Cell migration: integrating signals from front to back. *Science* 302: 1704–1709, 2003.
29. **Riveline D, Zamir E, Balaban NQ, Schwarz US, Ishizaki T, Narumiya S, Kam Z, Geiger B, and Bershadsky AD.** Focal contacts as mechanosensors: externally applied local mechanical force induces growth of focal contacts by an mDia1-dependent and ROCK-independent mechanism. *J Cell Biol* 153: 1175–1186, 2001.
30. **Sato M, Ozawa T, Inukai K, Asano T, and Umezawa Y.** Fluorescent indicators for imaging protein phosphorylation in single living cells. *Nat Biotechnol* 20: 287–294, 2002.
31. **Scherl A, Couté Y, Déon C, Callé A, Kindbeiter K, Sanchez JC, Greco A, Hochstrasser D, and Diaz JJ.** Functional proteomic analysis of human nucleolus. *Mol Biol Cell* 13: 4100–4109, 2002.
32. **Shroff SG, Saner DR, and Lal R.** Dynamic micromechanical properties of cultured rat atrial myocytes measured by atomic force microscopy. *Am J Physiol Cell Physiol* 269: C286–C292, 1995.
33. **Smith PG, Deng L, Fredberg JJ, and Maksym GN.** Mechanical strain increases cell stiffness through cytoskeletal filament reorganization. *Am J Physiol Lung Cell Mol Physiol* 285: L456–L463, 2003.
34. **Valberg PA and Albertini DF.** Cytoplasmic motions, rheology, and structure probed by a novel magnetic particle method. *J Cell Biol* 101: 130–140, 1985.
35. **Wang N, Butler JP, and Ingber DE.** Mechanotransduction across the cell surface and through the cytoskeleton. *Science* 260: 1124–1127, 1993.
36. **Wang N, Naruse K, Stamenović D, Fredberg JJ, Mijailovich SM, Tolić-Nørrelykke IM, Polte T, Mannix R, and Ingber DE.** Mechanical behavior in living cells consistent with the tensegrity model. *Proc Natl Acad Sci USA* 98: 7765–7770, 2001.
37. **Wang N, Tolić-Nørrelykke IM, Chen J, Mijailovich SM, Butler JP, Fredberg JJ, and Stamenović D.** Cell prestress: I. Stiffness and prestress are closely associated in adherent contractile cells. *Am J Physiol Cell Physiol* 282: C606–C616, 2002.
38. **Zhang J, Ma Y, Taylor SS, and Tsien RY.** Genetically encoded reporters of protein kinase A activity reveal impact of substrate tethering. *Proc Natl Acad Sci USA* 98: 14997–15002, 2001.